Master’s Thesis, 30 ECTS

Goniometric investigation of scattering from insect wings in near infrared

---

Division of Combustion Physics

Department of Physics

Faculty of Engineering LTH
Lund University

A thesis submitted in fulfillment of the requirements
for the degree of Master in Photonics
Project duration: January 2024- June 2024

Supervisors
Mikkel Brydegaard
Meng Li
Hampus Månefjord

Author
Emmanuel Kotu Robertson

June, 2024

Acknowledgement

I extend my heartfelt appreciation to the individuals listed below for their unwavering support throughout this project.

I extend my sincere appreciation to Mikkel Brydegaard for conceiving this intriguing project and demonstrating unwavering patience throughout its duration. His provision of essential tools, hospitality in the form of free drinks, and willingness to share his valuable experience, including German and Chinese lessons, have significantly contributed to our progress.

To Meng Li for her support throughout the project, valuable advice, and generous assistance especially in 3D printing. Her loan of a flash drive and dedication to printing my weekly findings have been invaluable. Moreover, her ability to infuse the project with a sense of enjoyment has made this endeavor truly memorable.

To Hampus Månefjord for providing the biospace rotation stage and his guidance on how use the biospace software. Also, for giving me access to all the relevant equipment in the laboratory.

To David Dreyer for his valuable input and advice throughout this project. His insights have been instrumental in shaping my progress, and I appreciate his support.

To Dolores Bernenko for sharing her MATLAB script that made my figures super nice.

To Jadanka Rota for providing the moths and hover fly specimens.

To Nina Reistad, who graciously lent me her spectrometer for my experiment. Her generosity and willingness to share her equipment made a significant impact on the success of my research.

Abstract

In recent decades, there has been significant attention on the decline in insect populations, including moths and hover flies. To tackle this issue, innovative methods such as entomological LiDAR technology have revolutionized the remote identification of free-flying insects. The distinct spectral reflection from moth and hover fly wings enables precise differentiation between species and sexes. While a comprehensive parameter space is crucial for accurate identification at the species and family levels, it's important to note that some parameters overlap. Consequently, incorporating more parameters would improve the identification accuracy of insect species.

This *ex-vivo* study investigates wing surface irregularities in moth and hover fly species by analyzing their short-wave infrared angular scattering properties in both the goniometric and spectral domains. These distinct wing surface irregularities can enhance the potential for discriminating between insect species.

The estimation of surface roughness involved fitting a Bidirectional Reflectance Distribution Function (BRDF) model to the angular scattering lobe. Subsequently, a short-pass function was applied to spectrally fit the surface roughness curve. The reflectance signals from moth and hover fly species were also effectively explained using a short-pass function. Notably, the retrieved wing surface heterogeneity and steepness remained consistent and offer valuable insights into the irregularities of wing surfaces.

The study reveals that both the angular scattering lobe and wing surface roughness increase toward visible wavelengths across all species. This information is valuable for researchers when selecting wavelengths for surface roughness studies. Additionally, the ventral side of the wings exhibits greater roughness compared to the dorsal side. This finding has practical implications for ground-based LiDAR technology, particularly when studying insect species with subdued spectral features, such as the ventral side of moth wings. Minimal surface roughness is associated with specular reflectance, resulting in lidar signals that exhibit numerous harmonic overtones. Overall, the results affirm that insect wings become more specular and smoother as wavelengths shift toward the infrared range.

Abbreviations

LiDAR	Light Detection and Ranging
BRDF	Bidirectional Reflectance Distribution Function
SWIR	Shortwave Infrared
BIOSPACE	Biophotonics, Imaging, Optical, Spectral, Polarimetric, Angular, and Compact Equipment
SEM	Scanning Electron Microscope
WISs	Wing Interference Signals
OCS	Optical Cross Section

Contents

Chapter 1

Introduction

1.1 Motivation behind this thesis

The ecological role of insects can not be ignored. Studies have reported a continuous decline of insect population in several countries. This decline has adverse effects on our ecosystem, and therefore a glowing concern for mankind. Most agricultural products which sustain life on earth today are largely attributed to insect pollinators. While insects help sustain the ecosystem, a fraction of insects population are pests and disease vectors which cause damage to agricultural crops and spread of disease respectively.

Entomologist for the past decades have been monitoring the behavior, population, and habitats of these insects using variety of approaches. However, the need to identify free-flying insects at the family and species level is becoming increasingly relevant as this information can be utilize for pest control and save pollinators and the natural ecosystem from the side effects of pesticides [1,2].

Entomological Light Detection and Ranging (LiDAR) is a powerful tool in biodiversity studies. Our research group has made advances in insect species identification research using advanced entomological LiDAR monitoring method, Scheimpflug lidar, with high spatiotemporal resoultion and sensitivity capable of monitoring insects' behavior, as well as disease vectors tracking.

Insect species identification studies are usually conducted in one or combination of polarimetric [3], spectral and frequency domains [4]. Measurement of wing beat frequencies (WBF) [5], harmonic overtones [6], Wing Interference Signals (WISs) [7] and techniques employing machine vision [8] and imaging can be used to potentially discriminate free-flying insect species. While the discrimination of species in the laboratory and close observation is simple, more research is essential to enhance the efficiency of remote identification of insect species [7].

1.2 State of the art

Numerous recent investigations employing a variety of techniques have sought to understand moth behavior. However, accurately identifying moths at the family and species levels remains a challenge using these methods. The reflection signal observed from moth wings, particularly on the ventral side, appears diffused due to the wing's dull coloration and becomes more pronounced at longer wavelengths. [9].

In a recent study on moths, researchers analyzed the spectral signals of twenty-six species within the range of 0.95 to 2.5 micrometers (µm). The findings were distilled into a set of complementary parameters that enhance the ability to discriminate between species. Notably, the investigation identified both quantitative and qualitative variations in moth wing nanostructures among species.

Figure 1.1a shows a Scanning Electron Microscope (SEM) image of the wing nanostructure of two moth species. Three periodic structures having different degrees of coarseness were seen. *M. strigula* and *F. bifida* were reported to have extreme values of surface roughness and steepness respectively among all the species studied, figure 1.1b. The report also confirms that the orientation of the wing has an insignificant influence on the surface roughness and steepness [9]. Such information can be used to discriminate moth species and possibly for remote identification of free flying insects.

According to [10] and [11], microstructures are capable of changing respectively the angular and infrared emissivity of an object. A study conducted by [12] has reveal a wavelength dependence of surface roughness. This dependence can be utilize to quantify the surface roughness of insects' wings which will significantly improve the chances of remotely identifying species of free-flying moths and hover flies.

The thickness of the wings has been confirmed to enable the identification of closely related hover flies species. The clear wings of hover flies are known to produce spectral fringes, or WISs, which depends on the thickness of the wing. Thinner wings are highly modulated and the modulation decreases as the effective thickness increases. Spectral fringes hold promise for discriminating between species and sexes of clear-winged insects with an impressive 91% accuracy [7]. However, despite the abundant parameter space available for species identification, there are some overlaps among these parameters. Further refinement by incorporating additional parameters is likely to enhance the accuracy of insect species identification. Particularly, the identification of moth and hover fly species based on wing surface roughness in the goniometric domain remains an unexplored research area.

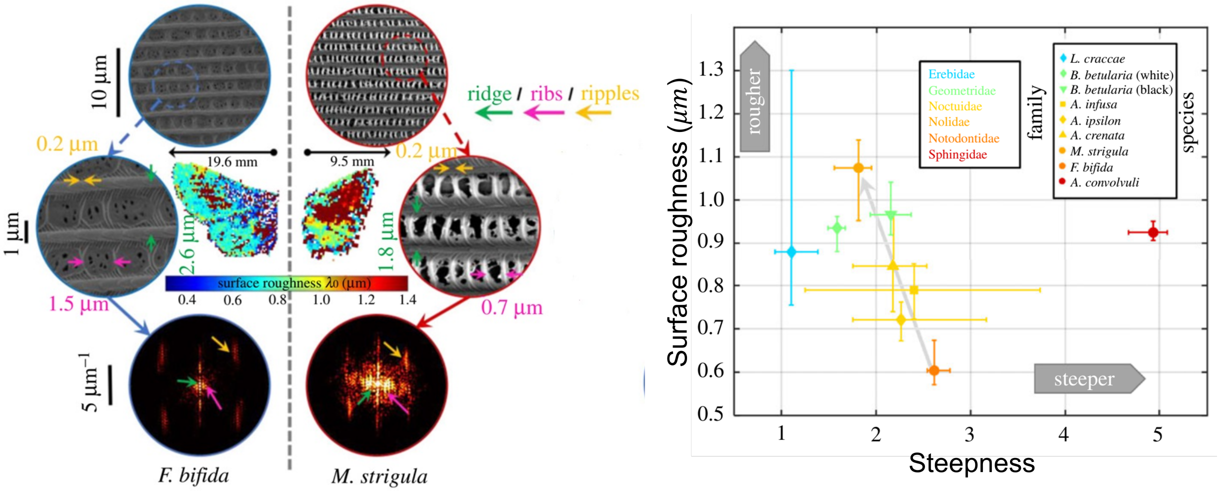

(a) (b)

Figure 1.1: (a) SEM images of extreme cases of moth wings of two moth species, (b) Summary of the surface roughnesses of moth species measured in the spectral and polarimetric domains [9]

1.3 Current Limitation

One major limitation in the context of entomological LiDAR studies on insect decline is the absence of accurate information on the angular distribution of light produced by free flying insects. Although the measured backscattered signal exhibits distinct harmonics [13] corresponding to wing beats, the exact angular spread remains unknown. The lack of precise knowledge regarding light distribution upon scattering by diverse insect species poses challenges in constructing comprehensive models and refining the accuracy of LiDAR measurements. Addressing this knowledge gap is essential for bolstering the reliability and effectiveness of entomological LiDAR systems in monitoring insect populations and decline.

1.4 Aim

The aim of this work is to investigate the angular scattering of Shortwave Infrared (SWIR) from various species of moth and hover fly wings in the goniometric domain. The primary objectives of this work include quantifying the surface roughness of moth and hover fly species using goniometric (Bidirectional Reflectance Distribution Function (BRDF)) and spectral models, understand the effect of wing surface roughness on angular scattering, and validate the angular scatter model proposed by Li et al. [9]. The research questions this work seeks to address are;

Research questions

1. How does the surface roughness change with wavelength of incidence light?
2. Does the angular scatter model proposed by Li et al., 2022 hold true and what are quantitative examples for surface roughness for hover flies and moths wings?
3. What is the difference in the angular spread between the reflectance of a clear wing and a scaled wings at SWIR?

1.5 Thesis outline

The thesis start with an introduction chapter which contains brief overview of insects and remote sensing, the current knowledge, aim and questions the research seeks to address. Chapter two is general theories relevant to this work. In chapter three, detailed account of the procedures and instrumentation are presented. Chapter four is dedicated to the analysis of the measured data and chapter five present all the results relevant to address the questions asked. Chapter six is reserved for discussion of the results and their significance to the scientific community. The last chapter concludes this work, suggestions and directions for future research and also included in this chapter.

Chapter 2

Theory

2.1 Light Scattering

Understanding the nature of light is of key relevance in LiDAR technology. This thesis is based on the backscattering of light from insect wings and only light-matter interactions relevant for this work is discussed in this section.

Insect wings play a significant role in the overall backscatter cross section, and this contribution exhibits an oscillatory behavior, unlike the scattering from the insect body. Most insect wings consists of a transparent chitin membrane with a thickness ranging from approximately 300 to 3000 nanometers. Additionally, a network of tubular veins enhances the wings' structural stiffness. Notably, the wings of moths and butterflies (Lepidoptera) feature microscopic scales [14].

Scattering occurs when light interact with these nano-features and deviates from its original propagation direction. This process depends on a number of factors including the size of the photonic structures, incidence angle and the wavelength of incident light. This study focuses on backscattering of SWIR light. By measuring the backscattered signal, size and surface roughness of insect wing can be retrieved [15]. In the subsequent subsections, detail interactions of the light and insect wings relevant to this work will be discussed.

2.1.1 Refractive index and Fresnel equations

Light traveling between media deviates from its original trajectory due to the change in refractive index.

Insect wings consist of thin film of chitin surrounded on both sides by air. They are responsible for the colored patterns of insect wings and thin-film interference in clear wing insects such as hover fly and mosquitoes. Another source of scattering from insect wings is the presence of melanin. Insects' bodies and wings contain a pigment called melanin, which absorbs short wavelengths [16].

Owing to the chitin's relatively high refractive index compared to that of air, incident light undergoes both reflection and refraction. Fresnel equations gives the fractions of reflected and transmitted electric fields to the electric field of the incident wave [17]. Only the reflectance part of Fresnel equations is relevant to this work. The Fresnel reflection coefficient consist of two linear polarization states, the *s* and *p* polarizations. The reflectivity of the surface is the average of the two reflectivities when an unpolarized light source is used since it has the same quantity of power in the *s* and *p* polarizations, equation 2.3.

$$R_s = \left(\frac{cos(\theta) - \sqrt{n_{chitin}^2 - sin^2(\theta)}}{cos(\theta) + \sqrt{n_{chitin}^2 - sin^2(\theta)}} \right)^2 \tag{2.1}$$

$$R_p = \left(\frac{\sqrt{1 - \left(\frac{sin(\theta)}{n_{chitin}}\right)^2} - n_{chitin} cos(\theta)}{\sqrt{1 - \left(\frac{sin(\theta)}{n_{chitin}}\right)^2} + n_{chitin} cos(\theta)} \right)^2 \tag{2.2}$$

$$R_{Fresnel} = \frac{R_s + R_p}{2} \tag{2.3}$$

Since biological interfaces are actually fractals at the nanoscale, surfaces are not perfectly flat, and subwavelength protruding structures would shift the scenario from Fresnel equations' refractive index step increase to one in which gradient refractive indices—also referred to as anti-reflectance coatings—occur [18].

2.1.2 Surface roughness

The wings of insects in the lepidoptera order such as moths and butterflies are covered by periodic micro- and nanostructured scales. In this work, surface roughness (denoted as (r)) represents a measurable parameter that characterizes the irregularities and deviations present on a wing's surface, distinguishing it from a perfectly smooth surface. The size and arrangement of scales on the wing surface differ between species and have different degree of roughness, figure 2.1a. By quantifying this roughness, the distinction between species can be further improved [9]. The degree of roughness depends on the wavelength of the incident light used.

Resolvable and Subwavelength structures

The scales on moths' wings are on the order of micro- scale. Resolving such features of the wing requires the wavelength of light used in the experiment to be relatively shorter than the size of the microstructures. Wavelengths in the visible range offer better lateral spatial resolution than wavelengths in the infrared range. When covering a wide range of wavelengths, certain nanoscale features may become subject to the resolution limit. Such nanoscale features or subwavelength structures appear almost flat to the incident beam and the surface roughness is not clearly resolved. The reflection from such a surface is specular in nature [19].

BRDF model

The surface roughness of resolvable structures on the wing surface can be quantified using the BRDF in equation 2.4. The model does not take diffraction and reflectance anisotropy from the repeating patterns resembling a grating structure on the scales into account [9, 12].

$$I(\theta,\varphi) = I_0(cos(F_{link}(\theta,(1-r)\theta_0)cos(F_{link}(\varphi,(1-r)\varphi_0)))^{1/r}, \tag{2.4}$$
$$r \in 0\ldots1$$

$$F_{link}(\theta,\theta_0) = 90^\circ\left(\left(\frac{\theta+90^\circ}{180^\circ}\right)^{\frac{-log(2)}{log\left(\frac{90^\circ-\theta_0}{180^\circ}\right)}} - \left(\frac{90^\circ-\theta}{180^\circ}\right)^{\frac{-log(2)}{log\left(\frac{\theta_0+90^\circ}{180^\circ}\right)}}\right) \tag{2.5}$$
$$\theta,\theta_0 \in -90^\circ\ldots+90^\circ$$

$$\iint_{-90^\circ}^{+90^\circ} I(\theta,\varphi)d\theta d\varphi = 1 \tag{2.6}$$

Where r is the surface roughness, θ and φ are the reflected pitch and roll directions. θ_0 and φ_0 are the incidence angles. A perfect mirror and a perfect diffusor has $r(\lambda) = 0$ and $r(\lambda) = 1$ respectively. BRDF gives the radiance to irradiance ratio for defined incident and scattered angles when light hit a sample surface [12].

2.1.3 Coherent and Incoherent scattering

Coherent scattering occurs when scattered light retains information about its original phase, direction, and polarization, whereas incoherent scattering lacks this memory [20]. If the wavelength remains the same after scattering then the scattering is considered elastic coherent, otherwise it is an inelastic coherent scattering [21]. The two light waves can interfere with each other constructively or destructively. Specular reflection is an example of coherent scattering. In incoherent scattering, the light is scattered in all possible directions regardless of the incident wavelength, and the phase relation between incident light wave and the scattered light is changed [22].

2.2 Specular and Diffuse reflection

The interaction between surface roughness and wavelength governs the degree of reflectance, distinguishing between specular and diffuse reflection. In specular reflection, the reflected photons contains information of their direction of incidence, and the incident and reflected light obeys the reflection laws. This type of reflection is coherent. In diffuse reflection, the incident light is reflected in various directions due to the roughness of the surface. When incident light enters and undergo multiple scattering inside a material, it loses its coherence with increasing number of interactions. After it exit the material from the illumination side, it is known as diffuse reflectance as shown in figure 2.1b.

In terms of wavelength of light, wavelengths towards infrared results in more specularity compared to visible wavelengths for the same surface roughness. This work uses SWIR light in the range of 930 nm to 1600 nm to study roughness of insect wings. This choice gives better spatial resolution which helps in characterizing the surface features of the wings.

2.3 Surface roughness and reflectance angular lobe for scaled wings

The angular lobe for diffused wing broadens with wing surface roughness towards visible wavelengths. That is, the reflectance signal becomes increasingly diffused when the wavelength of the incident light is shorter than the size of the structures of the surface of the wing. Moth wings are covered by scales composed of photonic structures that makes it rougher than clear-wing insects such as hover fly, and hence has larger angular reflectance lobe.

Figure 2.1a shows the dependence of scattering lobe on the surface roughness scaled to 100% simulated using the BRDF model of equation 2.4. The reflectance is specular for flat smooth surface and becomes increasingly diffused with surface roughness at the same incident angle.

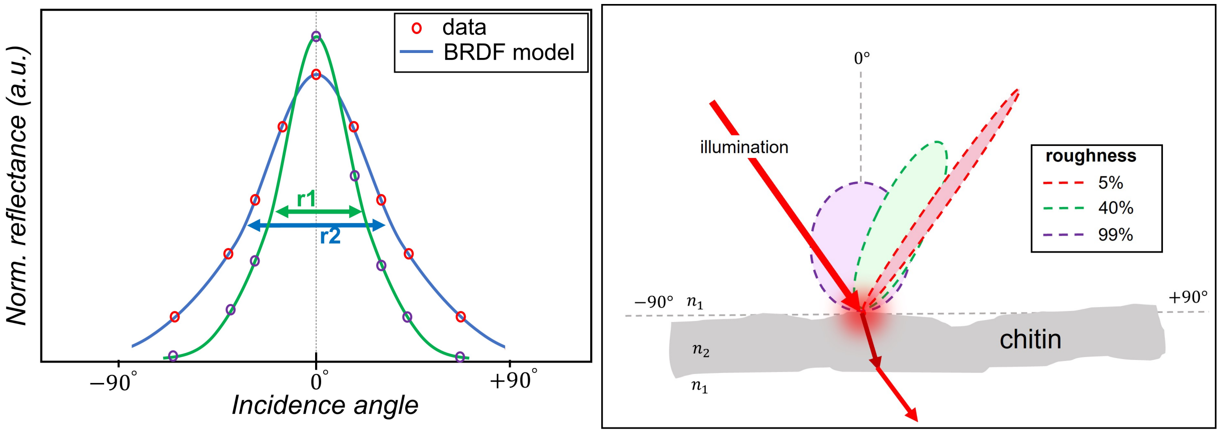

(a)

(b)

Figure 2.1: (a) BRDF definition of surface roughness (r1 < r2). Roughness (r) is the width of the angular scattering lobe. (b) A schematic of the angular scatter lobe for different degrees of surface roughness. Specular reflection lobe (red), diffuse scattering lobes (green and purple). n_1 and n_2 are the refractive indices of air and chitin respectively. Some of the light is transmitted.

2.4 Thin-film interference for clear wings

The wings of most insects have thickness ranging from approximately 300 to 3000 nanometers and mostly transparent [7]. In the simple case, these wings can be conceptualized as a single chitin slab with air on both sides, effectively forming a thin film. The wing is thicker at the fore edge and thinner at the hind edge [7]. When light is incident on such wings, it is reflected at both the front and rear surfaces in a specular manner. However, due to the thickness of the film, phase-shift is introduced as the light travels different path lengths. The reflected light then interfere in a phenomenon known as thin-film interference. In clear-wing insects such as hover fly, the reflection signal measured shows spectral fringes displaying high modulations towards infrared wavelength [23]. These spectral fringes are observed when the incident light is reflected in a specular manner by the wing membrane. The veins on the other hand cause diffuse scattering which does not contribute much to the fringes observed [7]. Constructive or destructive interference depends on the combination of a number of factors such as the angle of incidence, thickness of the layer, and wavelength of light, resulting in creation a colorful patterns on the wing surface [24]. Figure 2.2 illustrates thin-film interference.

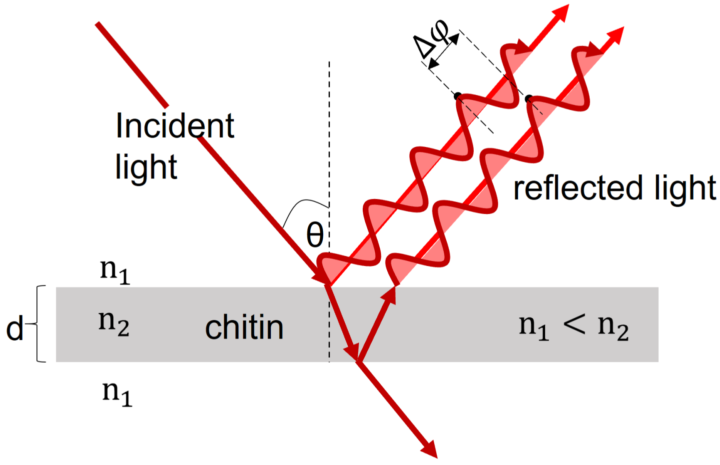

Figure 2.2: Thin film interference phenomenon. Reflected light from both surfaces have different phases. n_1 and n_2 are the refractive indices of air and chitin respectively.

2.4.1 Fringe model

Due to thin-film interference, the reflectance signal displays maxima and minima known as spectral fringes. A model has been developed which is capable of estimating the thickness of the thin wing from the spectral fringes [25]. However, the vein's contribution to the fringy signal is poorly explained by the finge model [7].

$$F(\lambda,d) = \frac{4R_{Fresnel} sin^2\left(2\pi d\sqrt{n^2 - sin^2\theta}/\lambda\right)}{(1-R_{Fresnel})^2 + 4R_{Fresnel} sin^2\left(2\pi d\sqrt{n^2 - sin^2\theta}/\lambda\right)} \tag{2.7}$$

Equation 2.7 is the fringe model. θ is incidence angle, d is the wing thickness, $R_{Fresnel}$ is Fresnel reflection coefficient, $n = A + B/\lambda^2$ is the refractive index of chitin with $A = 1.517$ and $B = 8800\,nm^2$ [18].

2.5 Relation between surface roughness and harmonics

Entomological LiDAR capitalizes on the optical characteristics of insect wings, where the specularity of these wings influences the modulation signals detected by the LiDAR system. Specifically, wings with a specular surface generate more pronounced harmonics in the power spectrum compared to rougher, diffuse wings. Understanding this relationship is pivotal for assessing how different wing types impact LiDAR signals [7]..

One notable phenomenon in entomological LiDAR is the “wing flash,” which occurs when the LiDAR beam aligns perpendicularly with the wing surface. This connection between surface roughness and harmonic generation plays a crucial role in optimizing LiDAR systems. For instance, selecting specific wavelengths that resonate with the thickness of clear wings or utilizing longer wavelengths within the SWIR range can enhance the specularity of even diffuse wings, resulting in more informative signals with increased harmonic content [7, 26].

2.6 Insect wing kinematics

The kinematics of insect wing when hovering and in forward flight can be explained with three euler angles [27, 28]. The stroke angle φ is the angle between the transverse axis and the wing position as it sweeps in the stroke plane, α is the wing pitch angle and θ is the deviation angle from the stroke plane [27]. The intricate kinematics of insect wings pose limitations for using LiDAR technology to remotely identify free-flying insects. This limitation arises primarily from the uncertainty surrounding the illumination angle, except in cases where a distinct flash occurs. Hence, backscattered signal is the most used method in LiDAR technology. Understanding the kinematics of insect flight is very essential for goniometric studies of free flying insects. Lepidopteran insects, in particular, have extremely complex wing kinematics due to the two pairs of wings’ intricate and difficult-to-replicate highly coordinated wing movements. In this work, the stroke position is fixed and the deviation angle is negligible, only the wing pitch angle is varied to study the backscattering properties of the wing surface. Figure 2.3 shows the parameters that describe the wing kinematics for mosquito.

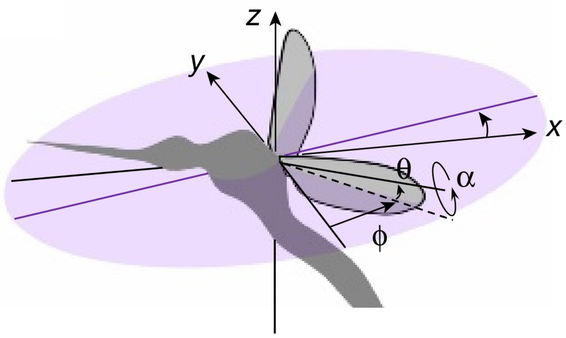

Figure 2.3: Flight kinematics of mosquito wing [27]

Chapter 3

Materials and Method

3.1 Instrumentation

3.1.1 Light source

The sample was illuminated by 12 volts, 20 watts broadband halogen lamp emitting light according to a 2300 K Planck curve. The area of the beam hitting the sample is approximately $210\,mm^2$. The lamp was powered by Switching Mode Power Supply with Rotary Encoder Control (HCS-3400) from Manson Engineering Industrial Ltd. A constant voltage of 9 V and current of 1.5 A was supplied to the lamp.

3.1.2 Sample stage

The sample stage was built with LEGO-technic. The stage is equipped with three servo motors to enable pitch and roll rotations of the insect wing. This insect wing rotation stage is a part of Biophotonics, Imaging, Optical, Spectral, Polarimetric, Angular, and Compact Equipment (BIOSPACE) design [29]. The servo motors (EV3 Medium Servo Motors, LEGO, Denmark) communicate with an open-source single-board computer (Raspberry Pi 4, Raspberry Pi Foundation, Cambridge, UK) through an add-on board (BrickPi3, Dexter Industries, Washington DC, United States).

3.1.3 Spectrometer

The detecting system is EPP2000-NIR-InGaAs Spectrometer with InGaAs Detector, 512 pixel cooled PDA array from StellarNet-Inc (Florida, 33626 USA). It has a range of 900 nm to 1600 nm, resolving resolution of 3.1 nm, f-number of 4, dynamic range of 4000:1 with 5 decades and pixel size of 25 μm x 500 μm.

3.1.4 Experiment setup

The experimental setup shown in figure 3.1 is designed to mimic entomological LiDAR technology. It consist of light source, condenser and objective lenses of focal lengths (FL) 75 mm and 200 mm respectively, insect wing rotation stage, a spectrometer and acquisition computer. The condenser lens (50 mm Dia, x 75 mm FL, NIR II Coated) and objective lens (50 mm Dia, x 200 mm FL, NIR II Coated) from Edmund optics have anti-reflection coating that offer negligible reflective loses in the $750\,nm - 1600\,nm$ wavelength range. The angle between the light source and the spectrometer θ_v is about 15°. The focusing angle of the objective lens γ is 7°, the convergence angle of the beam hitting the wing is 4°. The black case ($200\,mm \times 66\,mm \times 68\,mm$) that hold the lens was modelled using Computer-aided Design (CAD) software (Fusion 360, Autodesk, USA) to fit the focal length of the lens, and printed employing 3D printer (3D45, Dremel, USA). This allowed easy coupling of the signal to the spectrometer and shielding for glare and stray light that may affect the measurement accuracy. Similarly, another 3D printed black case ($40\,mm \times 66\,mm \times 68\,mm$) was used to hold the condenser lens 85 mm away from the light source to provide the required beam size. The largest half angle θ_s the condenser lens can collect light from the source is around 17°.

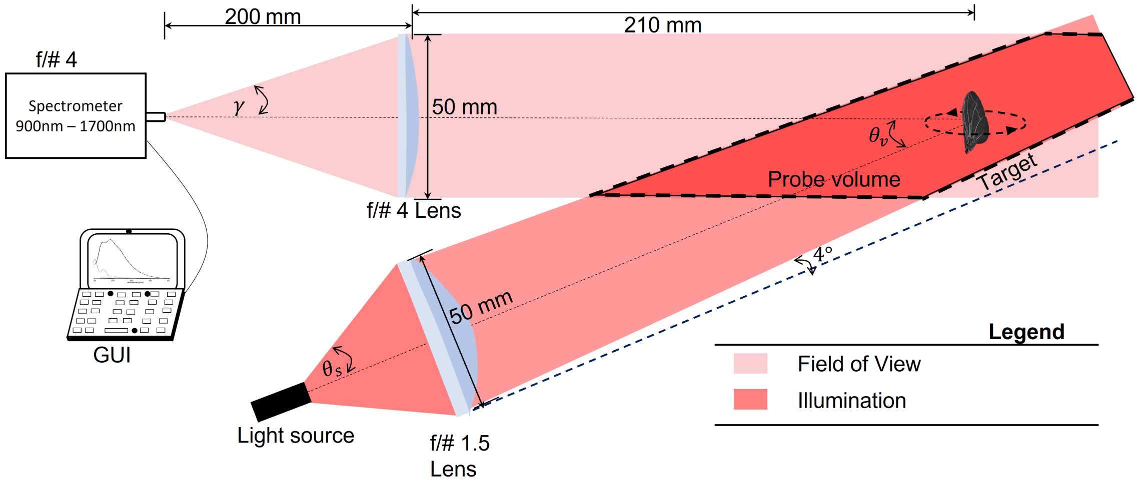

Figure 3.1: A schematic of the experiment setup

3.2 Sample

Moths and hover fly

Both the three hover fly and three moth species were provided by the Lund University Biological

Museum for this study. Moths and hover fly had been studied extensively. The samples were chosen because they present the extreme values of surface roughness, steepness and modulation that has been reported [7, 9]. Samples from moth species: *Aethalura punctulate*, *Furcula bifida* and *Meganola strigula*. From the Syrphidae family of hover fly: *Syritta pipiens* (♂), *Volucella bombylans* (♂) and *Xylota jakutorum* (♀) (see figure 3.2). Among the moth species, some wings exhibited a gentle flex, which couldn't be undone due to their fragility and the susceptibility of their surface scales to damage.

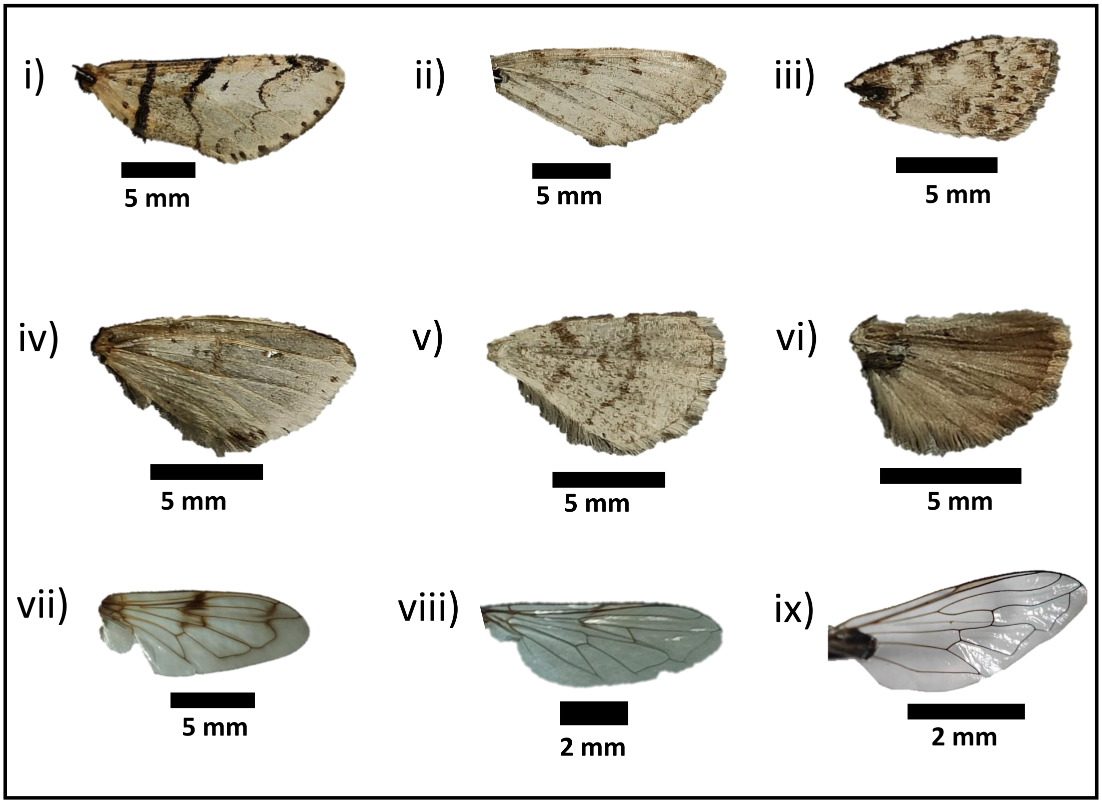

Figure 3.2: Three moth species and three hover fly species. First row: forewings of (i) *F. bifida*, (ii) *A. punctulate* and (iii) *M. strigula*. Second row: hindwings of (iv) *F. bifida*, (v) *A. punctulate* and (vi) *M. strigula*. Third row: hover fly wings (vii) *V. bombylans* (♂), (viii) *X. jakutorum* (♀), and (ix) *S. pipiens* (♂)

3.3 Experiment procedure

3.3.1 Pinning insect wings

The insect wings were carefully removed from the insect and pinned at the tip along the proximal-distal end of the wing by a glue. The insect pins used are black to reduce its effect on the backscattering signal. The pinned wings were labelled and placed vertically on a foam.

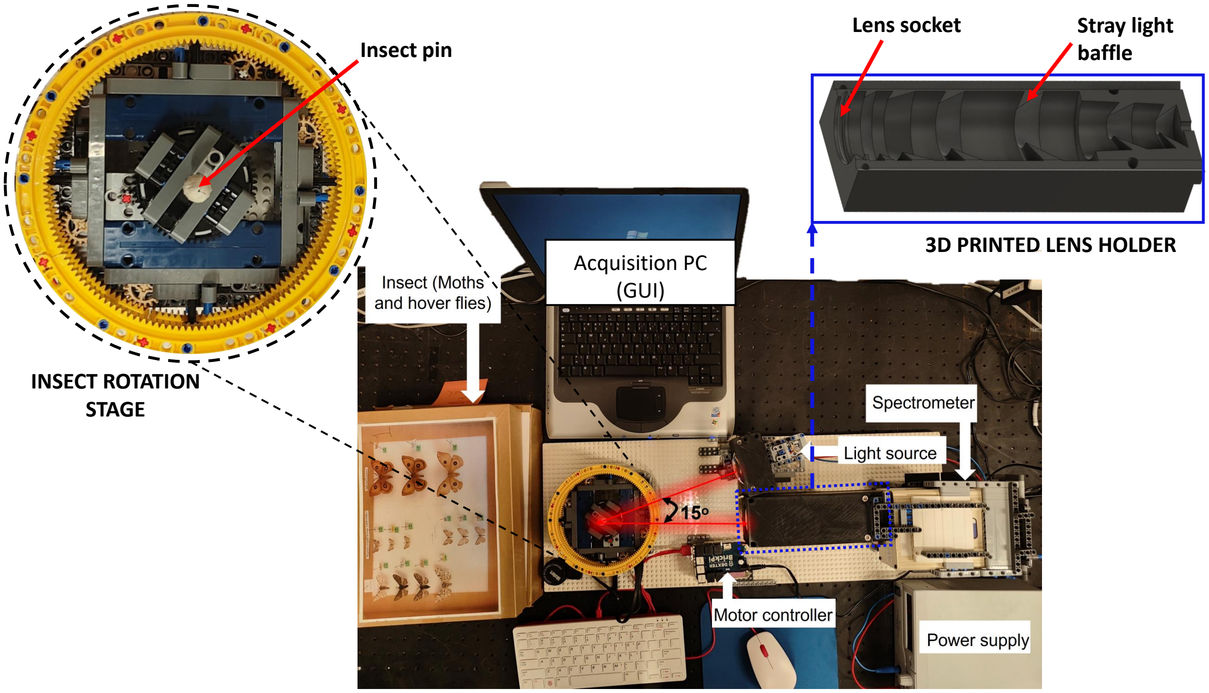

Figure 3.3: Experimental setup. The 3D printed lens holder (top right) is a half slice of the black case described above. The insect rotation stage is part of BIOSPACE platform. The motor controller is Raspberry Pi 4 [29].

3.3.2 Scanning the wings

The experiment was performed at 100 ms integration time and no signal averaging. A dark background followed by reference were measured for the calibration of the reflectance. The wings were vertically mounted on the rotation stage such that the whole area of the wing is illuminated.

The sample was rotated until maximum reflectance was found, which was labeled as zero degrees (normal). This is followed by scanning in one direction of the normal. The same steps were taking to scan in the other direction for both the dorsal and ventral sides of the wings. The light source and the spectrometer were fixed while the wings were rotated across the anterior-posterior axis of the wing, see figure 3.4. This method of scanning reduces uncertainty in the angles that results from mechanical noise of the servo motors. The same scanning angle range (-75° to 70°) was used for the three moth species. However, the scanning angles varied for the hover fly species. The spectral band used in this experiment is from 930 nm to 1600 nm at a resolution of 2.5 nm, given 268 bands.

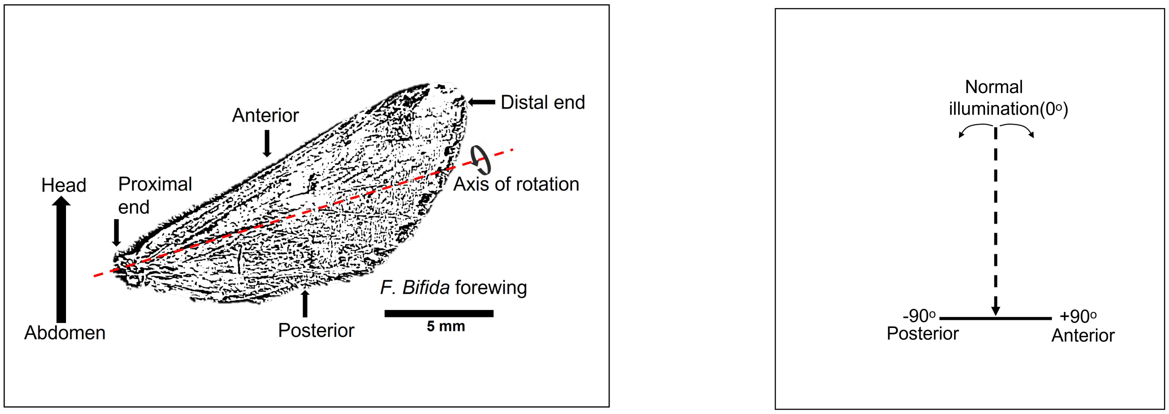

(a) (b)

Figure 3.4: (a) Insect wing label and scanning direction. The wing is pinned along the axis of rotation (red dashes). (b) The scanning angle direction from normal.

3.4 Calibrations

3.4.1 Reflectance calibration

The spectrometer used in the experiment comes with its own operating software, SpectraWIz. The software has an in-built function that calculate and display percent reflectance using the measured dark background, reference and current sample data sets according to equation 3.1 when the measurement is done in TRANS mode (transmission mode). However, the reference used in the experiment is Spectralon® Diffuse Reflectance Standards with a reflectance factor of 50%. Hence, the measured signal was multiplied by a factor 0.5. It is worth mentioning that signal integration time of $100\,ms$ was used throughout the experiment.

$$R(\lambda,\theta) = R_{ref}\frac{I_{sample}(\lambda,\theta) - I_{dark}(\lambda)}{I_{ref}(\lambda) - I_{dark}(\lambda)} \tag{3.1}$$

where R is backscattered reflectance as a function of wavelength (λ), and incidence angle (θ). I_{sample} is recorded intensities of scattered from the sample, I_{dark} is the recorded intensities without sample, I_{ref} is the recorded intensities of the grey reference.

3.4.2 Optical cross section calculation

The Optical Cross Section (OCS) of the wings was calibrated according to equation 3.2. OCS depends on the wavelength of the incident light and the angle of incidence. A reflection signal I_{ref} of a reference target of known surface area A_{ref} was measured and used to normalized scattered signals I_{sample} from the wings. This calibration is very useful for physical interpretation of results and sample comparison [15].

$$\sigma_{backscatter}(\lambda,\theta) = \frac{I_{sample}}{I_{ref}} A_{ref} \tag{3.2}$$

In order to better understanding the relationship between wavelength of incident light, incidence angle and OCS, contour filled plots were generated for every wing using `contourf` function in MATLAB.

3.4.3 Angular resolution calibration

The angular resolution of the setup was determined by measuring the full-width-half-maximum (FWHM) signal of a flat glass. The flat glass was illuminated normal to the surface for maximum signal, then it was rotated at small angular interval until the signal drop to less than half the maximum.

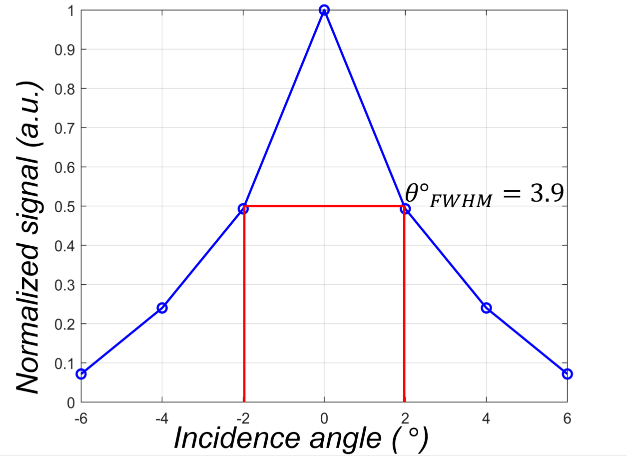

Figure 3.5: FWHM angular resolution of the experimental setup measured with flat glass.

Since the glass is smooth, it is assumed that by symmetric the angular reflectance is the same in both scanning directions. Using computer software such as MATLAB, the FWHM was estimated, see figure 3.5. The resolution was found to be approximately 4°. This resolution is good for goniometric measurement of rough surfaces since the angular increment in this experiment is higher than the angular resolution limit of the setup.

Chapter 4

Data Analysis

4.1 Data structure

The measured signal is automatically calibrated to reflectance measurements using equation 3.1. The first step was to convert all the files to MATLAB readable format.

This study involved six wing specimens from three moth species and three wing specimens from three hover flies. Each wing underwent scanning across a wavelength range of 930 nm to 1600 nm, with simultaneous measurements at 2.5 nm intervals, resulting in a dataset comprising 268 distinct wavelengths. Additionally, both the dorsal and ventral sides of forewings and hindwings for all moth specimens were meticulously scanned at 15 different incidence angles, spanning from $-75°$ to $+70°$. The reflectance data for each incidence angle were saved as separate files, resulting in a total of 180 reflectance files.

The three hover flies were measured for reflectance on both the dorsal and ventral sides. Specifically: *V. bombylans* was scanned at 15 incidence angles, ranging from $-60°$ to $+60°$. *X. jakutorum* underwent scanning at 13 incidence angles, spanning from $-45°$ to $+45°$. *S. pipiens* was scanned at 10 incidence angles, covering $-20°$ to $+30°$. As a result, a total of 76 reflectance files were saved. When combined with the moth measurements, we obtained 256 reflectance files across all 268 wavelengths.

The files were converted to `txt` format and orderly labelled for easy retrieval and analysis. Data analysis was performed using MATLAB, a programming language developed by MathWorks in the USA and licensed by Lund University. The analysis was done in the goniometric and spectral domains.

4.2 Goniometric model

Here, the aim is to quantify the wing surface roughness for both moth and hover fly wings using the BRDF model in equation 2.4. MATLAB script was written to fit the BRDF model using `lsqcurvefit` function from curve fitting toolbox and the surface roughness (r) for each wavelength (λ) was retrieved. The λ dependence of r appears to follow short pass function in the case of moth species, hence a short pass function was employed (equation 4.1) to spectrally fit r which is dependent on the incident angle θ and λ. The steepness α gives a better understanding of the effect of wavelength of incident light on the measured roughness of the surface. The maximum surface roughness that can be estimated with the BRDF model does not 100% which is also the case in practice. Therefore, λ_r is the cut-off wavelength.

$$R_s(\lambda) = \frac{1}{1+\left(\frac{\lambda}{\lambda_r}\right)^{\alpha}} \tag{4.1}$$

4.3 Spectral model

In the spectral model, the reflectance data for each angle of incidence is fitted separately to retrieve relevant information. A short-pass function in equation 4.3 was fitted to each reflectance data using robust fitting algorithm. Unlike moth's scaled wings, Hover flies' wings display spectral fringes so equation 4.2 was used to give a full description of its fringy nature. The fringe model also provide thickness of the wing information. λ_0 and β are the cut-off wavelength, which has dimension of length and gives information of the nanostructures of the wing surface and steepness of the slope respectively. This thesis report the fitting results of normal illumination.

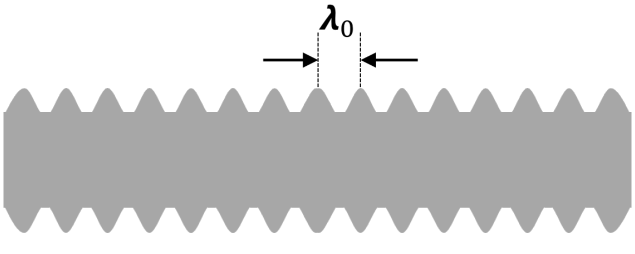

Figure 4.1: Definition of cut-off wavelength of the short pass function.

The reflectance model of the wing (R_{wing}) is obtained by multiplying the fringe model in equation 2.7 by short pass function.

$$R_{wing}(d) = R_s(\lambda)(R_{fringe} \cdot F_{(\lambda,d)} + R_{bias}) \tag{4.2}$$

R_{fringe} and R_{bias} are effective fringe amplitude and bias respectively. For wings that do not display fringes, $F_{(\lambda,d)}$ vanishes and the reflectance from the such wing is described by the bias term in combination with an appropriate physical model.

$$R_s(\lambda) = \frac{1}{1+\left(\frac{\lambda}{\lambda_0}\right)^{\beta}} \tag{4.3}$$

Chapter 5

Results

5.1 Goniometric model

Figures 5.1, 5.2, and 5.3 show the surface roughnesses of *F. bifida*, *A. punctulata*, and *M. strigula* respectively in goniometric domain at the wavelength range under study (930 nm - 1600 nm). Polar plot of two wavelengths are also reported, (a) and (b). The contour plot of the OCS at all angles is shown in (c) and (b). The BRDF fitting was done for each wavelength and only the mean adjusted R-squared (R^2_{adj}) for both the dorsal and ventral sides of the wings are shown in *red* and *green* colors respectively.

In figures 5.1, 5.2 and 5.3, the surface roughness of moth wings increases towards visible wavelengths for all species of moths' wing studied. The angular scattering lobe was consistently broader at $980\,nm$ than at $1550\,nm$.

The results indicate that the ventral side of most wings is rougher than the respective dorsal side. The distinct surface roughness observed among species on the ventral side of the wing has promising implications for ground-based vertical LiDAR applications. However, the dorsal side of the hindwing of *A. punctulata* is rougher at infrared wavelength as seen in figures 5.2.

The scattering lobes for all the species were measured to be symmetric, and therefore only one side is presented for both the polar plot and the contourf plot. Again, in figures 5.1, 5.2, and 5.3, the top and down parts of both the polar plot (horizontal through the center) and the contourf plot (separated by white dashes) are respectively the dorsal and ventral sides of the wings.

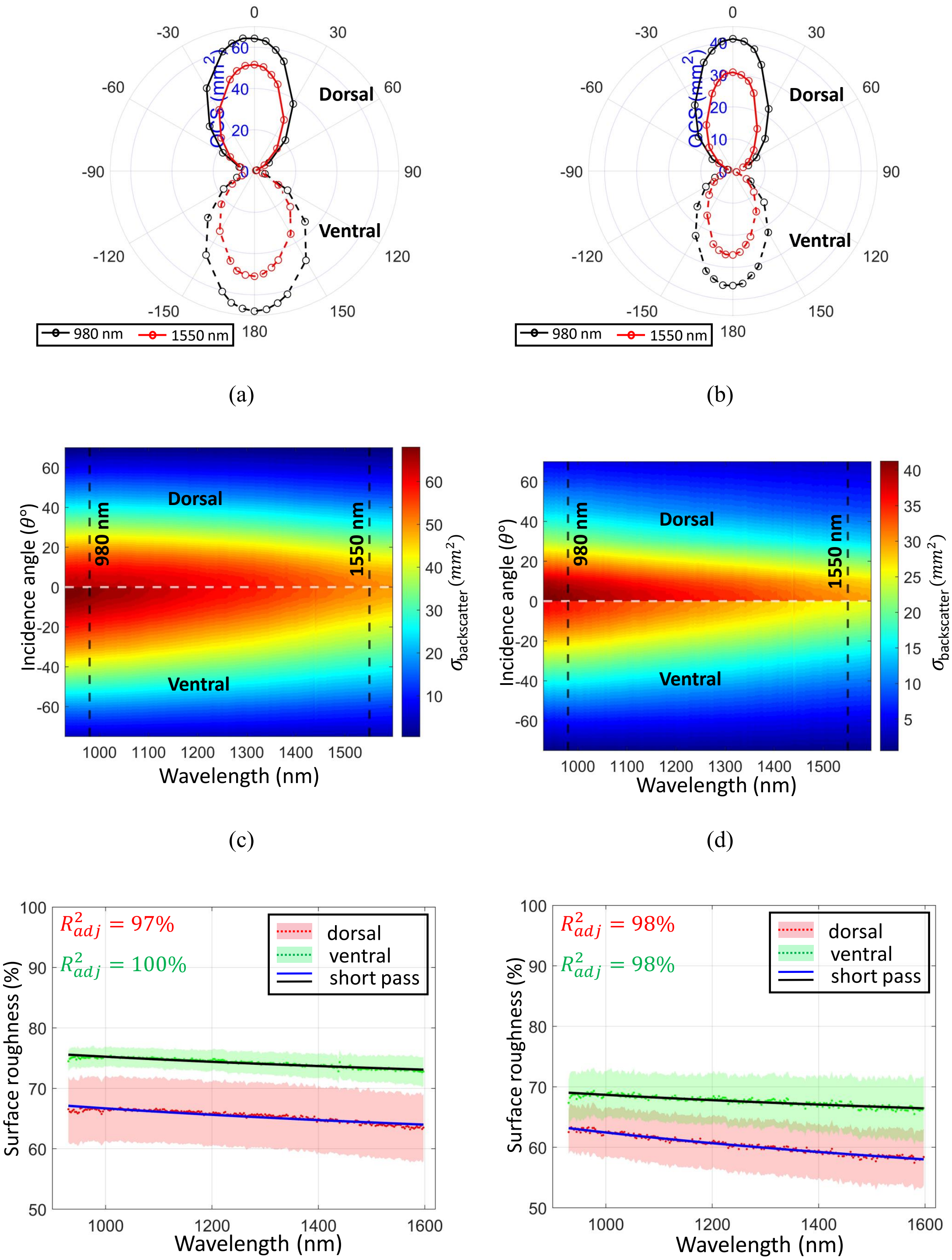

(a) (b)

(c) (d)

(e) (f)

Figure 5.1: The result for *F. bifida*. (a) and (b) are angular scattering lobes of fore- and hindwings respectively at 980 nm and 1550 nm. (c) and (d) are OCS distribution of fore- and hindwings respectively. (e) and (f) are surface roughness of fore- and hindwings respectively. The shaded area is the confidence interval of the surface roughness. The mean R^2_{adj} shown is color coded for the two surface roughness curves. Power model is shown by blue and black solid lines.

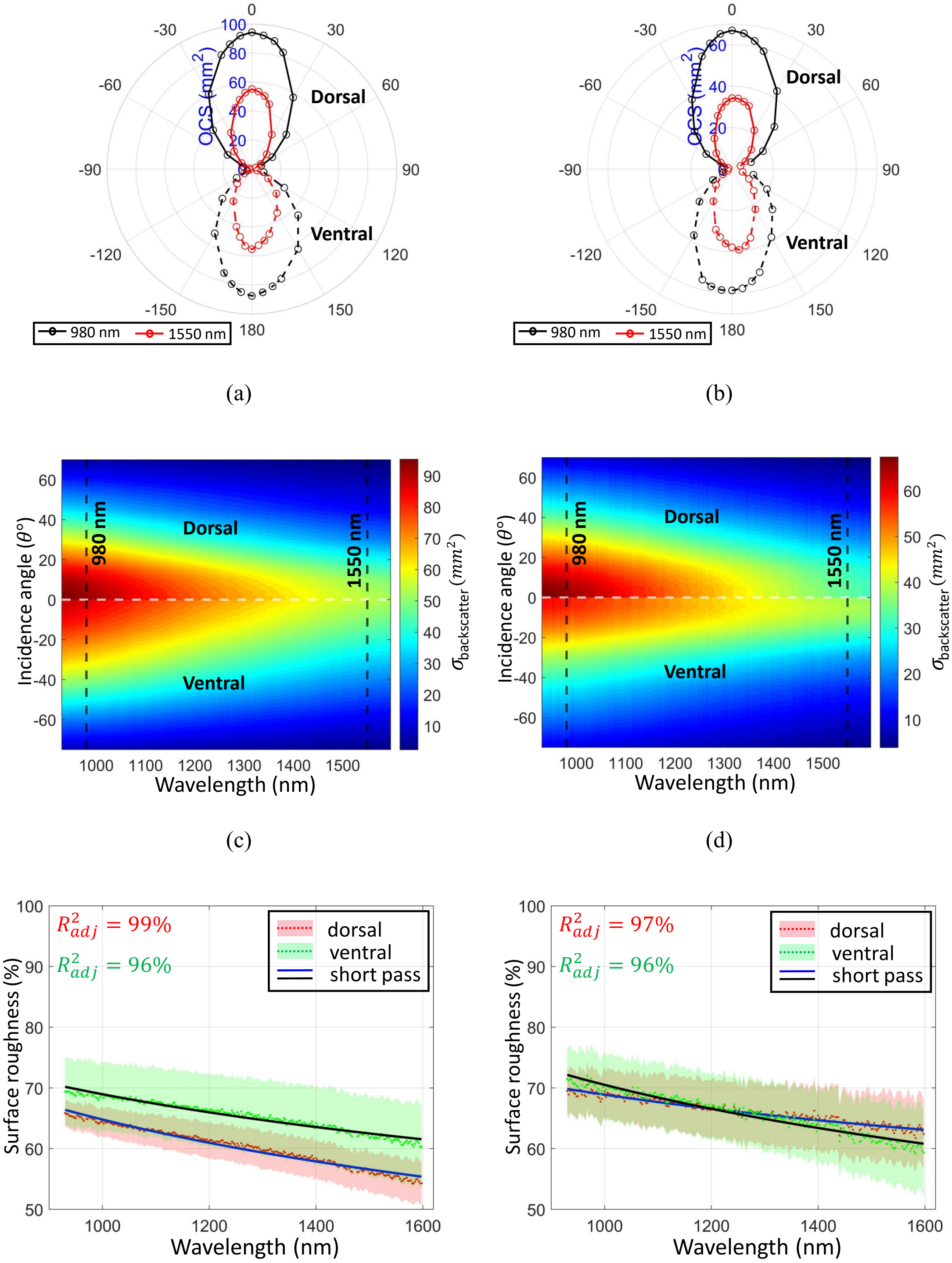

(a) (b)

(c) (d)

(e) (f)

Figure 5.2: The result for *A. punctulata*. (a) and (b) are angular scattering lobes of fore- and hindwings respectively at 980 nm and 1550 nm. (c) and (d) are OCS distribution of fore- and hindwings respectively. (e) and (f) are surface roughness of fore- and hindwings respectively. The shaded area is the confidence interval of the surface roughness. The mean R^2_{adj} shown is color coded for the two surface roughness curves. Power model is shown by blue and black solid lines.

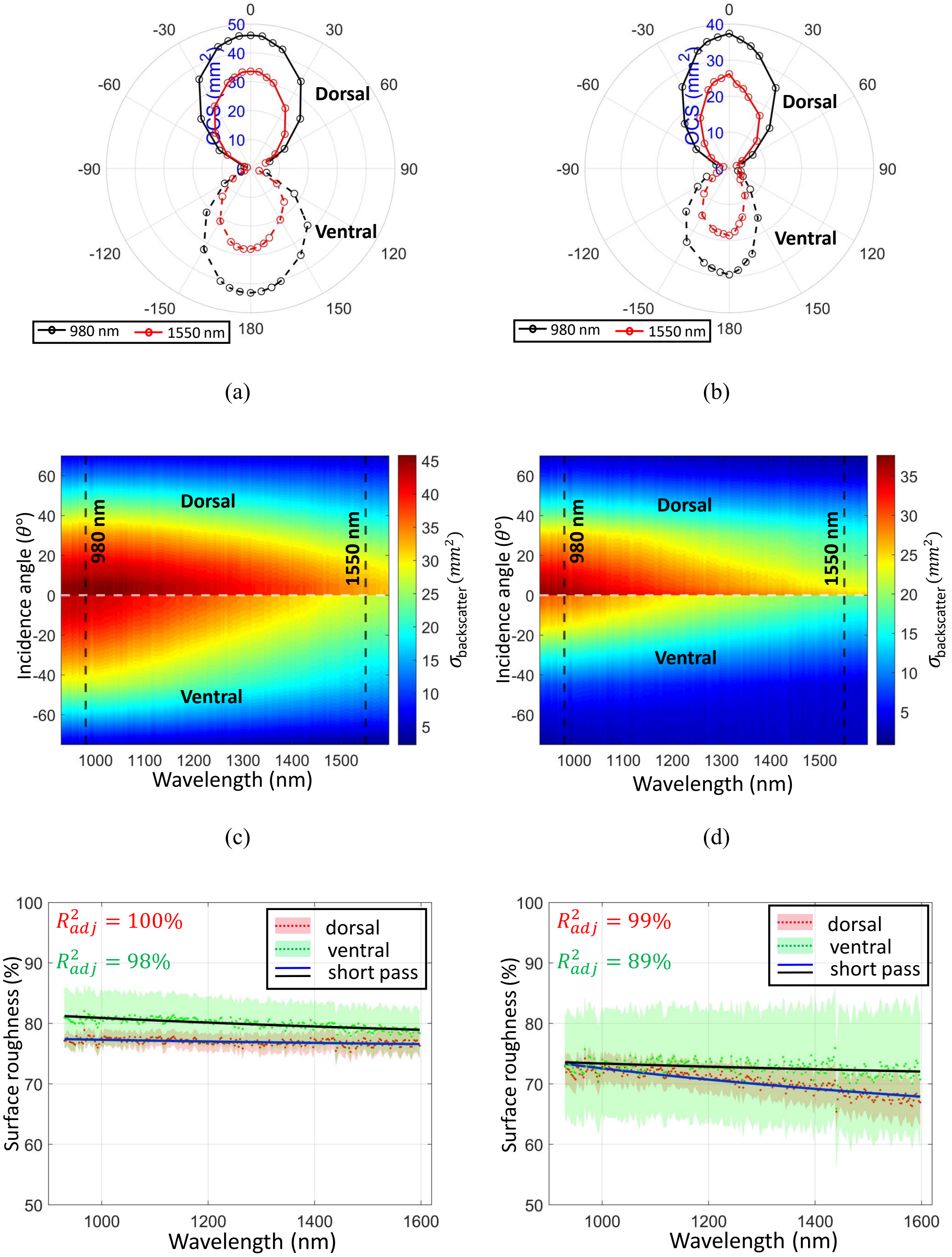

(a) (b)

(c) (d)

(e) (f)

Figure 5.3: The result for *M. strigula*. (a) and (b) are angular scattering lobes of fore- and hindwings respectively at 980 nm and 1550 nm. (c) and (d) are OCS distribution of fore- and hindwings respectively. (e) and (f) are surface roughness of fore- and hindwings respectively. The shaded area is the confidence interval of the surface roughness. The mean R^2_{adj} shown is color coded for the two surface roughness curves. Power model is shown by blue and black solid lines.

Figure 5.4 shows the surface roughness of the dorsal and ventral sides of hover fly wings. To understand the relation between the wing surface roughness and the fringes seen in the spectra of hover fly wings, the OCS results at (0°) illumination angle was shown in the same figure for easy comparison. The OCS data show variations in surface roughness across the wing and the corresponding spectral fringes' intensity and spacing.

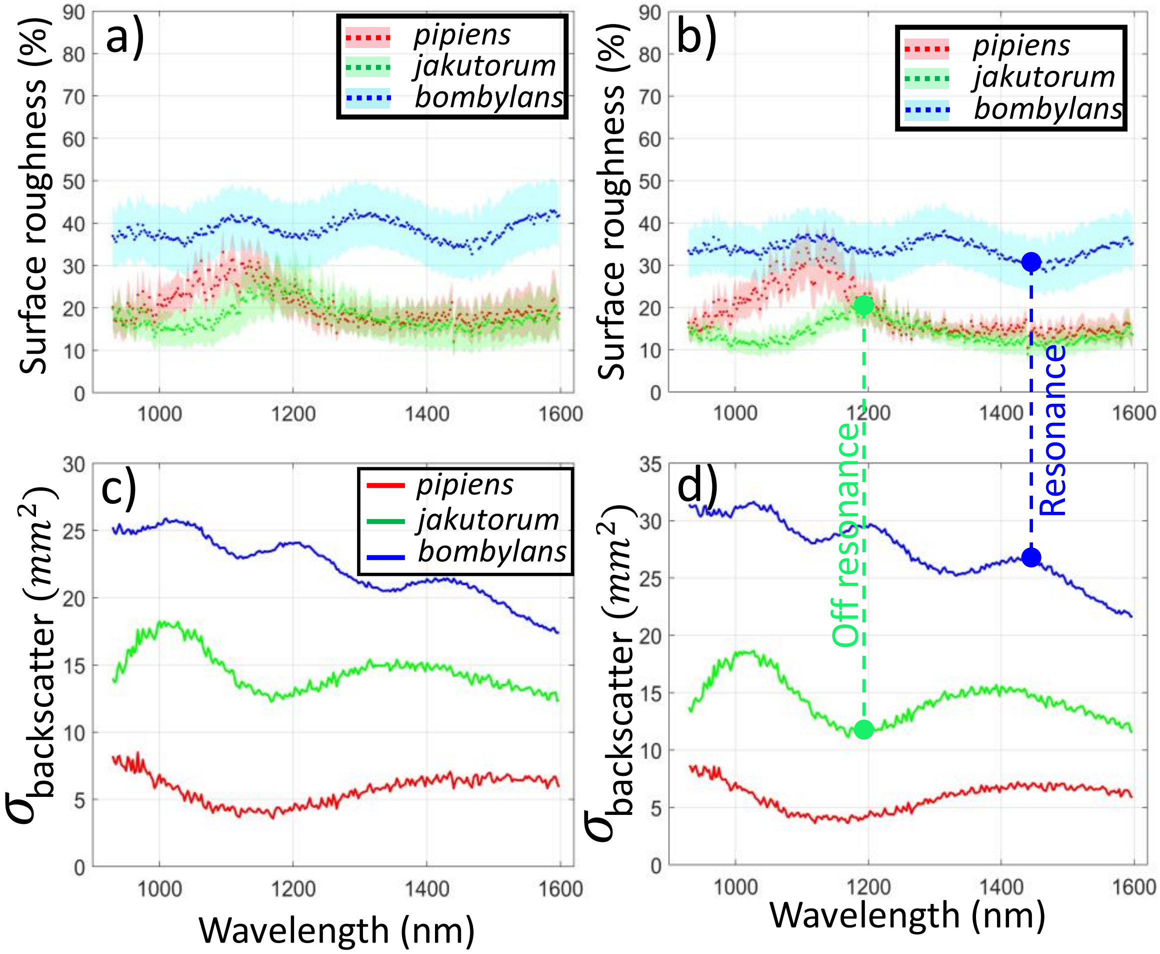

Figure 5.4: Relationship between the estimated surface roughness (a,b) and reflectance (c,d) of clear wing insects. (a,c) is the dorsal side and (b,d) is the ventral side of the hover fly wings. The surface roughness rises at off resonance. The drop of the reflectance signal is due to diffuse scattering by the wing veins which causes destructive interference. Hence, the veins are largely responsible for the measured surface roughness.

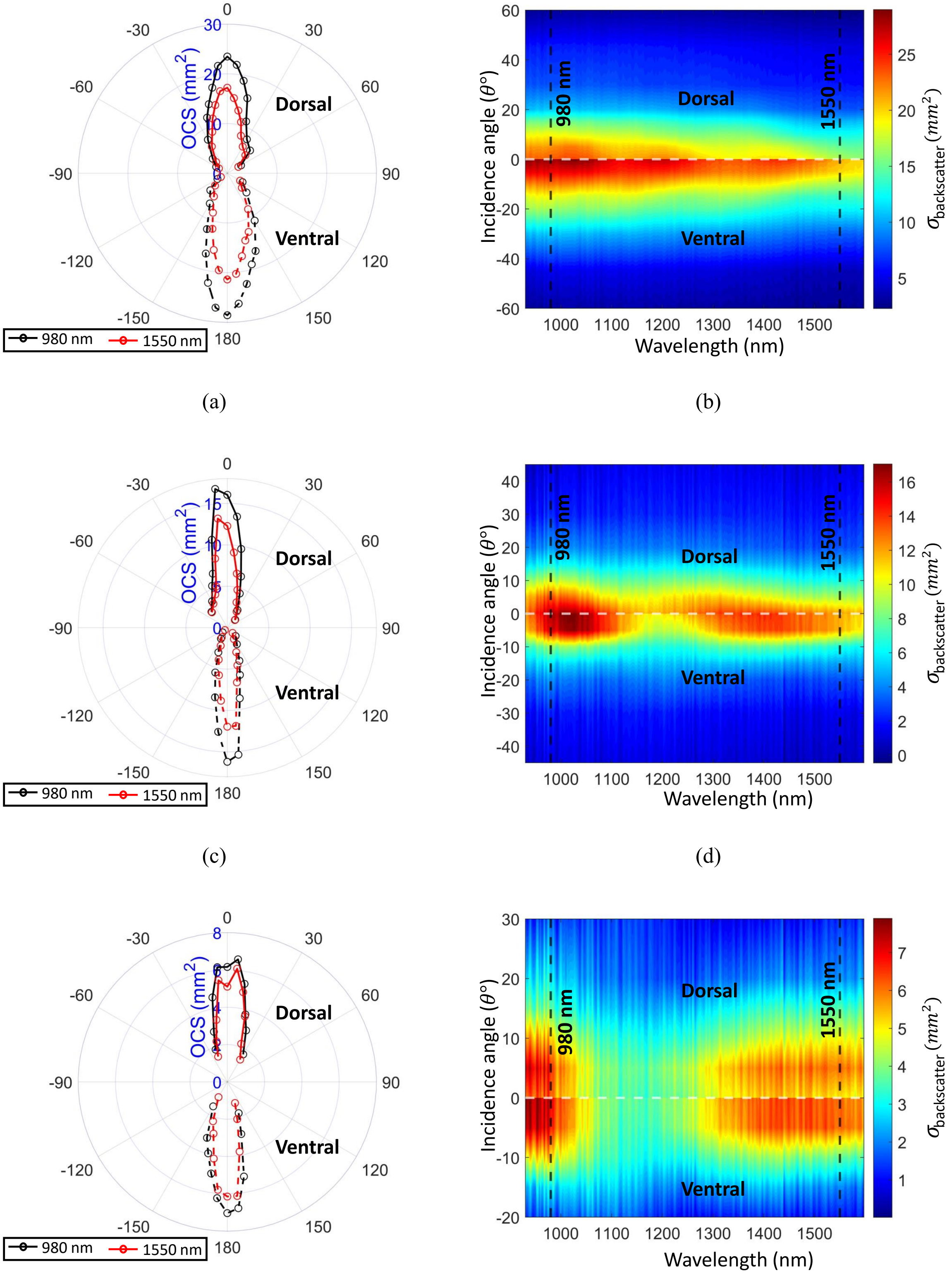

(a) (b)

(c) (d)

(e) (f)

Figure 5.5: Angular scattering lobes and OCS distribution of *V. bombylans*: (a,b), *X. jakutorum*: (c,d), *S. pipiens*: (e,f) measurements

Figure 5.5 displays the polar plots of the angular distribution and the OCS colormap for the three hover fly species. The OCS colormap illustrates the spectral fringes, where the x-axis represents wavelength, the y-axis represents the incident angle, and the intensity of the fringes is represented by the color scale. *V. bombylans* wing being the thickest shows the least fringe modulation [7]. *S. pipiens* shows a more distinct fringe modulation because it has the thinnest wing among the three species.

The surface roughness of hover fly wings is higher when there is a destructive interference (figure 5.4). The results from the polar plot for all species affirm that the surface of the wing appears glossier towards infrared wavelengths [9]. The result also shows that the wings of moth species studied are all significantly rougher than the hover fly wings.

5.2 Spectral model

The reflectance of the wing model described in equation 4.2 for the estimation of wing surface roughness (λ_0) and steepness (β) fitted well to the fringy signal of hover fly wings with averaged R^2_{adj} of 96%. The result from the spectral model is shown in figure 5.6. The cut-off wavelength λ_0 of clear wings of hover fly species is consistently larger compared to that of scaled-wings of moth species.

The steepness of *F. bifida* wing's backscattered signal in figure 5.6a shows that the signal rises less steeply towards visible wavelengths, while that of *M. strigula* wings show close to linear relation and *A. punctulata* rises steeply. The three hover fly species' wings have high steepness values for backscattering signal towards visible wavelengths, 5.6b. Aside from *A. punctulata*, the ventral side of all the wings studied, both moths and hover flies, scatter light more than their dorsal side characterize by their steepness.

The result of the short pass fitting of the surface roughness from goniometric model is shown in figures 5.1, 5.2, and 5.3 (e) and (f), as red and blue solid lines. The short pass function could fit the surface roughness data from moth wings with high (R^2_{adj}) values. However, the dorsal side of the forewing of *M. strigula* was poorly explained by the short pass function with R^2_{adj} of 22%. The short pass function could not properly fit the surface roughness of hover fly wings due to its fringy nature which is expected from clear wings (see figure 5.4). The data retrieve from the short pass function and R_{wing} fitted to backscattered reflectance are presented in the tables 5.1,5.2, 5.3 and 5.4.

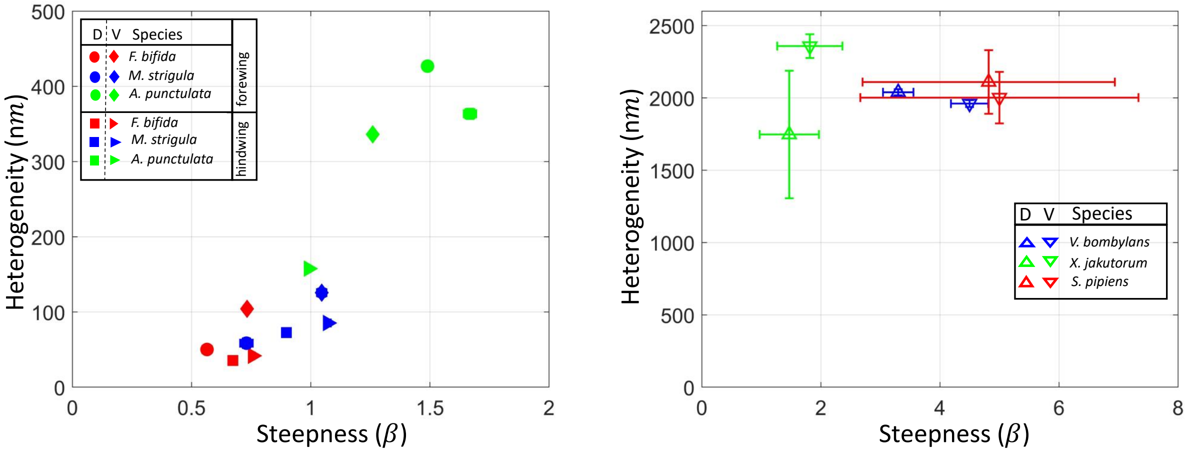

(a) (b)

Figure 5.6: Fringe heterogeneity (λ_0) plotted against steepness (β) in the spectral model for moths (a) and hover fly (b). D and V in the legend represent dorsal and ventral sides of the wing respectively. Short-pass function was fitted to the moth's wings reflectance signal. The hover fly wings' reflectance was fitted using the model described in equation 4.2.

Spectral	Reflectance short-pass model					
Forewing	**Dorsal**			**Ventral**		
Species	$\lambda_0(nm)$	β	$R^2_{\text{adj}}(\%)$	$\lambda_0(nm)$	β	$R^2_{\text{adj}}(\%)$
F. bifida	50 ± 5.5	0.57 ± 0.02	91.8	104 ± 4.5	0.73 ± 0.02	98.1
A. punctulata	427 ± 2.5	1.49 ± 0.01	99.8	336 ± 2.5	1.26 ± 0.01	99.8
M. strigula	59 ± 6.5	0.73 ± 0.03	91.3	126 ± 5.5	1.05 ± 0.02	97.5

Table 5.1: Spectral short-pass fit parameters of zero degree illumination for moths' forewing.

Spectral	Reflectance short-pass model					
Hindwing	**Dorsal**			**Ventral**		
Species	$\lambda_0(nm)$	β	$R^2_{\text{adj}}(\%)$	$\lambda_0(nm)$	β	$R^2_{\text{adj}}(\%)$
F. bifida	36 ± 1.5	0.67 ± 0.01	99.1	42 ± 1.5	0.76 ± 0.01	99.3
A. punctulata	364 ± 6.5	1.67 ± 0.03	98.3	158 ± 2.5	0.99 ± 0.01	99.6
M. strigula	73 ± 2.0	0.90 ± 0.01	99.3	85 ± 2.5	1.07 ± 0.01	99.1

Table 5.2: Spectral short-pass fit parameters of zero degree illumination for moths' hindwing.

Dorsal	**Reflectance of the wing model: short pass**					
Species	$\lambda_0(nm)$	β	$R_{bias}(\%)$	$R_{fringe}(\%)$	$d(\mu m)$	$R^2_{\text{adj}}(\%)$
V. bombylans	1961 ± 12	4.50 ± 0.31	5.6 ± 0.1	1.5 ± 0.2	2.15 ± 0.01	97.6
X. jakutorum	2358 ± 82	1.81 ± 0.55	3.7 ± 0.4	11.6 ± 1.0	1.17 ± 0.01	98.0
S. pipiens	2002 ± 178	5.00 ± 2.34	1.0 ± 0.1	4.6 ± 0.3	0.75 ± 0.01	90.0

Table 5.3: Spectral reflectance of the wing model parameters of zero degree illumination for the dorsal side of hover flies' wing.

Ventral	**Reflectance of the wing model: short pass**					
Species	$\lambda_0(nm)$	β	$R_{bias}(\%)$	$R_{fringe}(\%)$	$d(\mu m)$	$R^2_{\text{adj}}(\%)$
V. bombylans	2039 ± 21	3.30 ± 0.26	7.2 ± 0.1	1.4 ± 0.2	2.16 ± 0.01	98.1
X. jakutorum	1747 ± 441	1.47 ± 0.50	3.8 ± 0.8	15.3 ± 3.0	1.18 ± 0.01	98.2
S. pipiens	2110 ± 220	4.82 ± 2.12	0.9 ± 0.1	6.4 ± 0.3	0.75 ± 0.01	96.2

Table 5.4: Spectral reflectance of the wing model parameters of zero degree illumination for the ventral side of hover flies' wing.

5.3 Combined model

Figure 5.7 combines the mean surface roughnesses at all wavelength range from the goniometric model and the steepness (α) from the spectral power model that was fitted to the surface roughness from BRDF model. The moth species studied shows high degree of surface roughness compared to hover fly species. However, their wavelength dependence of surface roughness characterize by their α is between zero and one. This implies that the surface roughness curves rise less steeply towards visible wavelengths.

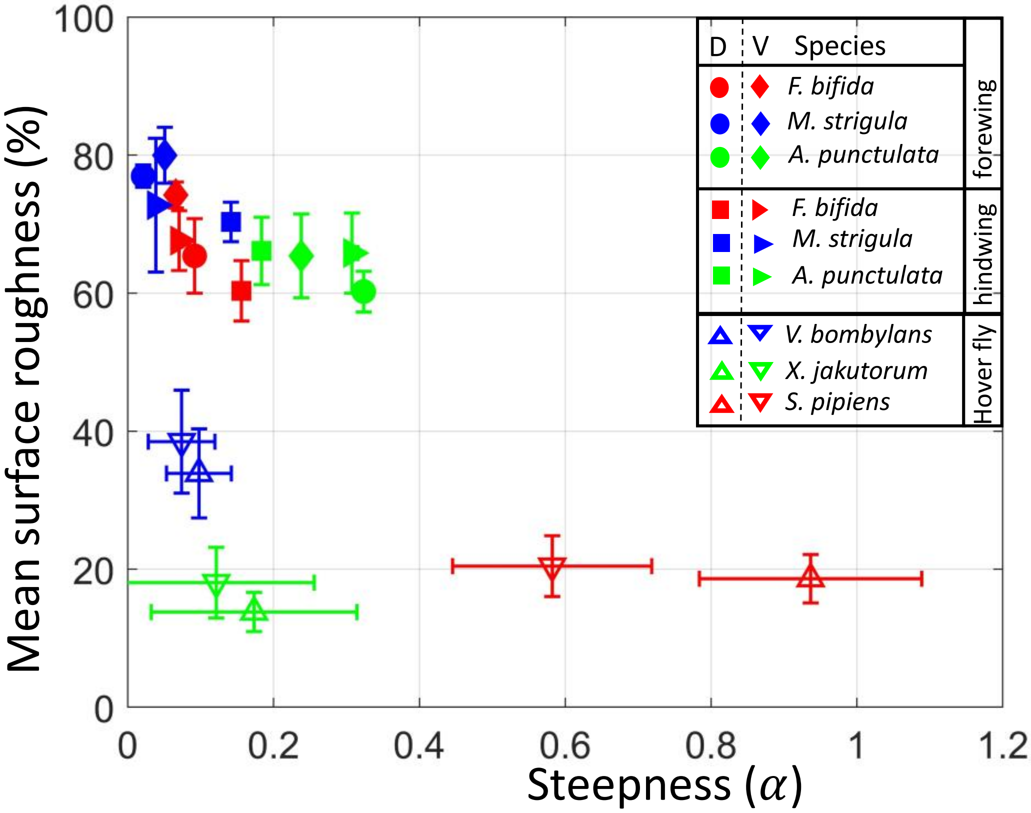

Figure 5.7: Mean surface roughness from goniometric model plotted against steepness from power model for both moths and hover fly species. *D* and *V* in the legend represent dorsal and ventral sides of the wing respectively.

Chapter 6

Discussion

6.1 Goniometric model

Both the backscattered reflectance and the subsequent surface roughness estimated using the BRDF model for all the insect wings increase towards short wavelengths (see the polar plots in result chapter). This can be seen when the polar plots of all the species are compared to their surface roughness parameters. The polar plots also reveal that the angular scattering lobe of diffused wing such as moth wings is broader than the angular scattering lobe of clear wings of hover fly at the same wavelength. The surface of *M. strigula* wings is much rougher than that of *F. bifida*. This observation adds more weight to the report from previous study [9].

The BRDF model was able to quantify the surface roughness of *A. punctulata* wings which previously could not be estimated [9]. While the idea of using mean surface roughness for moth and hover fly species comparison may not always provide accurately information due to the surface roughness across the spectral range having different steepness values, it is a good approximation in this case where there are obvious differences between the surface roughness values of the species studied. Another important observation made in the case of moth wings is the fact that the surface of the ventral side of all the wings are rougher than their respective dorsal side especially towards visible wavelengths. The coloration of ventral side of moth wings are dull so the prospects of discriminating them using their spectral signatures are limited. Hence, the ability to discern variations in surface roughness, which exhibit significant differences across species, enhances the potential for remote identification of insect species using ground-based LiDAR technology.

In figure 5.4, the variations in surface roughness across the wing, as indicated by the OCS data, are inversely correlated with the intensity and spacing of the fringes in the spectral measurements. The surface roughness of thin wings are more pronounce towards visible wavelengths since infrared wavelengths see an increase in fringe modulation [7,30]. The vein tubes are responsible for mostly diffuse scattering by thin wings, which is more significant towards visible wavelengths while wing membrane is responsible for specular reflection [7]. The findings from this work confirm the validity of the angular scatter model proposed by Li et al. [9].

Longer wavelengths are generally expected to scatter primarily in a specular fashion at normal incidence, while shorter wavelengths should scatter more diffusely because of their sensitivity to surface irregularities. However, the unexpected observation of intense scattering towards visible wavelengths at normal incidence, predominantly for moths' wings, contradicts this conventional understanding. The underlying hypothesis is that longer wavelengths can go through the wing, resulting in a relatively small backscattered reflectance of the longer wavelengths compared to shorter wavelengths.

6.2 Spectral model

6.2.1 Moths

The result of fitting the short-pass function to the backscattered signal has been shown in figure 5.6. Here, the discussion centers on the cut-off wavelengths and their significance to the wing surface roughness. A smaller cut-off wavelength implies that the surface scatters more successfully towards visible wavelengths. This corresponds to high spatial frequency nanostructures on the surface (see figure 4.1). The result from the goniometric model has shown that large surface features characterized by their closeness to each other (i.e. high spatial frequencies) scatters light more efficiently towards visible wavelength. Hence, smaller cut-off wavelength should mean rougher surface. The result after applying the short-pass function shows that the nanostructures on the scales of *F. bifida* wings have high spatial frequency. The findings align with the scanning electron microscopy (SEM) images obtained during the moth study, revealing that F. bifida exhibits the most pronounced lateral periodicity [9]. The short pass function successfully explain the backscattered reflectance with an average accuracy of 96%.

6.2.2 Hover flies

The observed cut-off wavelengths for hover fly wings in figure 5.6b exhibit some overlap. Consequently, definitive conclusions regarding the dorsal or ventral side of the wings cannot be drawn conclusively. To enhance confidence and address potential sources of error, additional data measurements from multiple individuals are necessary. However, the observed cut-off wavelengths for hover fly wings consistently exceed those of moth wings, indicating that moth wings exhibit greater roughness compared to hover fly wings.

Chapter 7

Conclusion and Outlook

In this work, the angular scattering of SWIR from three species each of moths and hover flies in the goniometric and spectral domains were investigated. The research focused on understanding the relation between wing surface roughness and angular scattering lobe from 930 nm to 1600 nm wavelength range.

The angular scattering lobe for all the insect species becomes broader towards visible wavelengths even for clear wing insects. Two extreme wavelengths, 980 nm and 1550 nm highlight this finding. Surface roughness decrease towards infrared wavelengths. This result is consistent across all the moth species indicating that short wavelengths are capable of interaction with smaller features on the wing surface which are not visible to longer wavelengths. This affirm that towards infrared moth wing becomes smooth and specular. The angular scattering lobe becomes broader with increasing wing surface roughness for both moth and hover fly species. The ventral side of the moth wings are much rougher than the dorsal side. This enhances the potential of remote identification of moth species with ground-based LiDAR technology.

The surface nanostructures of moth and hover fly wings were investigated by fitting short-pass function to the data and retrieving their cut-off wavelengths. This work also emphasizes the utility of SWIR light for ecological monitoring and remote sensing of insects; by choosing suitable wavelengths, one can improve the identification and description of insect populations through their scattering signatures. Finally, the results from confirms that the angular scatter model proposed by Li et al. is accurate.

Future work could examine diverse insect species and environmental factors to yield a more all-encompassing comprehension of SWIR scattering. Additionally, since sunlight can be ultilized to retrieve spectral features of insects, the wavelength range used in this work can be extended to the visible range. Finally, A more sophisticated rotation stage or other mechanisms that can offer more degrees of freedom would be advantageous to include in order to approximate the wing kinematics of insects more closely.

Bibliography

[1] Nesreen M Abd El-Ghany, Shadia E Abd El-Aziz, and Shahira S Marei. A review: application of remote sensing as a promising strategy for insect pests and diseases management. *Environmental Science and Pollution Research*, 27(27):33503–33515, 2020.

[2] Klas Rydhmer, Emily Bick, Laurence Still, Alfred Strand, Rubens Luciano, Salena Helmreich, Brittany D Beck, Christoffer Grønne, Ludvig Malmros, Knud Poulsen, et al. Automating insect monitoring using unsupervised near-infrared sensors. *Scientific Reports*, 12(1):2603, 2022.

[3] Yiyun Li, Zehua Han, Reed Nessler, Zhenhuan Yi, Philip Hemmer, Robert Brick, Alexei V Sokolov, and Marlan O Scully. Optical multiband polarimetric modulation sensing for gender and species identification of flying native solitary pollinators. *Iscience*, 26(11), 2023.

[4] Mikkel Brydegaard and Sune Svanberg. Photonic monitoring of atmospheric and aquatic fauna. *Laser & Photonics Reviews*, 12(12):1800135, 2018.

[5] Ilyas Potamitis and Iraklis Rigakis. Measuring the fundamental frequency and the harmonic properties of the wingbeat of a large number of mosquitoes in flight using 2d optoacoustic sensors. *Applied Acoustics*, 109:54–60, 2016.

[6] Mikkel Brydegaard, Benoit Kouakou, Samuel Jansson, Jens Rydell, and Jeremie Zoueu. High dynamic range in entomological scheimpflug lidars. *IEEE Journal of Selected Topics in Quantum Electronics*, 27(4):1–11, 2021.

[7] Meng Li, Anna Runemark, Julio Hernandez, Jadranka Rota, Rune Bygebjerg, and Mikkel Brydegaard. Discrimination of hover fly species and sexes by wing interference signals. *Advanced Science*, 10(34):2304657, 2023.

[8] Roel Van Klink, Tom August, Yves Bas, Paul Bodesheim, Aletta Bonn, Frode Fossøy, Toke T Høye, Eelke Jongejans, Myles HM Menz, Andreia Miraldo, et al. Emerging technologies

revolutionise insect ecology and monitoring. *Trends in ecology & evolution*, 37(10):872–885, 2022.

[9] Meng Li, Clara Seinsche, Samuel Jansson, Julio Hernandez, Jadranka Rota, Eric Warrant, and Mikkel Brydegaard. Potential for identification of wild night-flying moths by remote infrared microscopy. *Journal of the Royal Society Interface*, 19(191):20220256, 2022.

[10] Wei Li and Shanhui Fan. Nanophotonic control of thermal radiation for energy applications. *Optics express*, 26(12):15995–16021, 2018.

[11] Xianliang Liu, Talmage Tyler, Tatiana Starr, Anthony F Starr, Nan Marie Jokerst, and Willie J Padilla. Taming the blackbody with infrared metamaterials as selective thermal emitters. *Physical review letters*, 107(4):045901, 2011.

[12] Roman Basistyy, Adrien Genoud, and Benjamin Thomas. Backscattering properties of topographic targets in the visible, shortwave infrared, and mid-infrared spectral ranges for hard-target lidars. *Applied optics*, 57(24):6990–6997, 2018.

[13] Mikkel Brydegaard and Samuel Jansson. Advances in entomological laser radar. *The Journal of Engineering*, 2019(21):7542–7545, 2019.

[14] Mary K Salcedo, Jordan Hoffmann, Seth Donoughe, and L Mahadevan. Computational analysis of size, shape and structure of insect wings. *Biology Open*, 8(10):bio040774, 2019.

[15] Samuel Jansson. *Entomological lidar: target characterization and field applications*. PhD thesis, Lund University, 2020.

[16] Niels P Kristensen, Malcolm J Scoble, and OLE Karsholt. Lepidoptera phylogeny and systematics: the state of inventorying moth and butterfly diversity. *Zootaxa*, 1668(1):699–747, 2007.

[17] Richard O Prum and Rodolfo Torres. Structural colouration of avian skin: convergent evolution of coherently scattering dermal collagen arrays. *Journal of Experimental Biology*, 206(14):2409–2429, 2003.

[18] Doekele G Stavenga. Thin film and multilayer optics cause structural colors of many insects and birds. *Materials Today: Proceedings*, 1:109–121, 2014.

[19] DH Ranguin. *Subwavelength structured surfaces: theory and application*. PhD thesis, Ph. D. dissertation (University of Rochester, Rochester, New York, 1993), 1993.

[20] Marissa Goerke, Zbigniew Ulanowski, Georg Ritter, Evelyn Hesse, RR Neely, Laurence Taylor, RA Stillwell, and PH Kaye. Characterizing ice particles using two-dimensional reflections of a lidar beam. *Applied optics*, 56(19):G188–G196, 2017.

[21] Andrey V Romanov and Maxim A Yurkin. Single-particle characterization by elastic light scattering. *Laser & Photonics Reviews*, 15(2):2000368, 2021.

[22] Fouad El-Diasty. Coherent anti-stokes raman scattering: Spectroscopy and microscopy. *Vibrational Spectroscopy*, 55(1):1–37, 2011.

[23] Meng Li, Anna Runemark, Noélie Guilcher, Julio Hernandez, Jadranka Rota, and Mikkel Brydegaard. Feasibility of insect identification based on spectral fringes produced by clear wings. *IEEE Journal of Selected Topics in Quantum Electronics*, 29(4: Biophotonics):1–8, 2022.

[24] Klas Rydhmer. Insects in the spotlight -photonic monitoring of bees and insect diversity, phd thesis, copenhagen university. 2023.

[25] Haiwei Yin, Lei Shi, Jing Sha, Yizhou Li, Youhua Qin, Biqin Dong, Serge Meyer, Xiaohan Liu, Li Zhao, and Jian Zi. Iridescence in the neck feathers of domestic pigeons. *Physical Review E*, 74(5):051916, 2006.

[26] Mikkel Brydegaard. Advantages of shortwave infrared lidar entomology. In *Laser Applications to Chemical, Security and Environmental Analysis*, pages LW2D–6. Optica Publishing Group, 2014.

[27] Richard J Bomphrey, Toshiyuki Nakata, Nathan Phillips, and Simon M Walker. Smart wing rotation and trailing-edge vortices enable high frequency mosquito flight. *Nature*, 544(7648):92–95, 2017.

[28] Alexander P Willmott and Charles P Ellington. The mechanics of flight in the hawkmoth manduca sexta i. kinematics of hovering and forward flight. *Journal of experimental Biology*, 200(21):2705–2722, 1997.

[29] Hampus Månefjord, Meng Li, Christian Brackmann, Nina Reistad, Anna Runemark, Jadranka Rota, Benjamin Anderson, Jeremie T Zoueu, Aboma Merdasa, and Mikkel Brydegaard. A biophotonic platform for quantitative analysis in the spatial, spectral, polarimetric, and goniometric domains. *Review of Scientific Instruments*, 93(11), 2022.

[30] Lauro Müller, Meng Li, Hampus Månefjord, Jacobo Salvador, Nina Reistad, Julio Hernandez, Carsten Kirkeby, Anna Runemark, and Mikkel Brydegaard. Remote nanoscopy with infrared elastic hyperspectral lidar. *Advanced Science*, 10(15):2207110, 2023.